

**P2-Na<sub>2/3</sub>Mg<sub>1/4</sub>Mn<sub>7/12</sub>Co<sub>1/6</sub>O<sub>2</sub> cathode material based on oxygen redox activity with improved first-cycle voltage hysteresis**

Nuria Tapia-Ruiz<sup>1,2,4,\*</sup>, Cindy Soares<sup>2</sup>, James W. Somerville<sup>1</sup>, Robert A. House<sup>1,4</sup>, Juliette Billaud<sup>3</sup>, Matthew R. Roberts<sup>1</sup> and Peter G. Bruce<sup>1,4,\*</sup>

<sup>1</sup>Departments of Materials and Chemistry, University of Oxford, Parks Road, Oxford OX1 3PH, UK.

<sup>2</sup>Department of Chemistry, Lancaster University, Lancaster LA1 4YB, UK.

<sup>3</sup>Electrochemistry Laboratory, Paul Scherrer Institut (PSI), 5232 Villigen, Switzerland.

<sup>4</sup>The Faraday Institution, Quad One, Becquerel Avenue, Harwell Campus, Didcot, OX11 0RA, UK

**Abstract**

The recent report of P2-Na<sub>2/3</sub>Mg<sub>0.28</sub>Mn<sub>0.72</sub>O<sub>2</sub> (P2-NMM) demonstrated the possibility of utilizing the oxygen redox couple in a layered oxide cathode without the need for alkali ions or vacancies in the transition metal layer. In this work, we report the synthesis of a new P2-type compound, Na<sub>2/3</sub>Mg<sub>1/4</sub>Mn<sub>7/12</sub>Co<sub>1/6</sub>O<sub>2</sub> (P2-NMMC), which exhibits reversible specific capacities as high as 173 mAh g<sup>-1</sup> and an improvement of the first cycle voltage hysteresis over P2-NMM. The material was characterised using a combination of ex-situ and operando techniques including X-ray diffraction (XRD), differential electrochemical mass spectrometry (DEMS) and X-ray absorption spectroscopy (XAS) to identify potential sources for this improvement.

**Introduction**

Recently, there has been an urgent need for the utilisation of renewable sources such as solar and wind to reduce the carbon footprint<sup>1</sup>. The inherent intermittent behaviour of these sources has driven an increasing market demand towards large stationary energy storage systems that can store energy generated during off-peak hours to meet the peak-hour demand. The high production costs of lithium combined with their limited geographical distribution have directed the attention to the development of alternative cheaper and more accessible rechargeable metal-ion battery systems such as sodium-ion batteries (SIBs)<sup>2,3</sup>. However, the replacement of lithium for sodium comes at the expense of a reduction in energy density due, in part, to the higher standard potential of Na<sup>+</sup> compared to Li<sup>+</sup> (-2.71 V cf. -3.04 V vs. standard hydrogen electrode (SHE)).

One of the main routes to improving the energy density in SIBs is by designing positive electrode (cathode) materials, being sodium layered transition metal oxides (Na<sub>x</sub>MO<sub>2</sub>, 0 < x ≤ 1 and M = 1<sup>st</sup>-row transition metal)<sup>4</sup>, among the most promising candidates. These layered materials mainly crystallise into either O3, P2 or P3-type structures, depending on whether the sodium ions occupy octahedrally (O) or trigonally prismatic (P) coordinated sites between the *n* [MO<sub>2</sub>] layers in the unit cell. In P2-type materials, sodium ions are coordinated to oxygen in a trigonal prismatic environment, sharing edges and faces with the [MO<sub>2</sub>] layer, leading to an ABBA stacking (Figure 1a). Even though there has been an extensive amount of literature related to P2-type compounds, studies have mainly focussed on materials that charge-compensate the sodium ion (de)intercalation by a redox reaction centred on the transition metal. After previous findings on oxygen redox reactions occurring in Li-rich transition metal oxides explained by ionic Li<sup>+</sup>-O(2p)-Li<sup>+</sup> interactions<sup>5,6</sup>, research has been directed to the exploration and understanding of anionic reactions occurring in P2-type compounds. For

instance, Meng et al. synthesised the high sodium content ( $x > 2/3$ ) and transition metal (TM) deficient P2-Na<sub>0.78</sub>Ni<sub>0.23</sub>Mn<sub>0.69</sub>O<sub>2</sub>, and observed an irreversible excess capacity of 60 mAh g<sup>-1</sup>, which they attributed to oxygen-based redox processes<sup>7</sup>. Later, Maitra et al. using the P2-Na<sub>2/3</sub>Mg<sub>0.28</sub>Mn<sub>0.72</sub>O<sub>2</sub> (P2-NMM) material first reported by Komaba et al.<sup>8</sup>, demonstrated that oxygen redox does not require alkali metals/undercoordinated oxygen to exhibit reversible capacity<sup>9</sup>. The authors also showed evidence for the absence of oxygen evolution during cycling, unlike in typical Li-rich type materials<sup>5</sup> and compounds with 4d and 5d TM<sup>10,11</sup>.

Herein, inspired by the oxygen redox capability observed in the P2-NMM material, we report the synthesis and characterisation of the layered P2-Na<sub>2/3</sub>Mg<sub>1/4</sub>Mn<sub>7/12</sub>Co<sub>1/6</sub>O<sub>2</sub> (P2-NMMC) material. P2-NMMC has a lower content of redox-inactive Mg<sup>2+</sup> ions, which leads to the lack of ordering in the TM layer, and the substitution of the Mn<sup>3+</sup>/Mn<sup>4+</sup> redox-active couple by the higher voltage Co<sup>3+</sup>/Co<sup>4+</sup> couple. The high capacity observed in the material on the first charge, (162 mAh g<sup>-1</sup>), was mainly attributed to an anionic redox reaction (ca. 112 mAh g<sup>-1</sup>). An improved average discharge voltage in the first cycle compared to the P2-NMM material<sup>8,9</sup> was also observed. Reducing the first cycle hysteresis of O-redox materials is desirable for real-world application<sup>12,13</sup>. A combination of ex-situ and operando techniques including operando X-ray diffraction (XRD), differential electrochemical mass spectrometry (DEMS) and X-ray absorption spectroscopy (XAS) were used to gain further insight into the structural and charge compensation mechanisms occurring in the electrode material during cycling.

## **Experimental Section**

### **Material Synthesis**

P2-Na<sub>2/3</sub>Mg<sup>(II)</sup><sub>1/4</sub>Mn<sup>(IV)</sup><sub>7/12</sub>Co<sup>(III)</sup><sub>1/6</sub>O<sub>2</sub> (P2-NMMC) was prepared by ball milling a stoichiometric mixture of Na<sub>2</sub>CO<sub>3</sub> (Sigma Aldrich, BioXtra, ≥ 99.0%), MgO (Sigma Aldrich, -325 mesh, ≥ 99% trace metal basis), Co<sub>3</sub>O<sub>4</sub> (Alfa Aesar, 99.7% trace metal basis) and MnO<sub>2</sub> (Sigma Aldrich, -325 mesh, 99%) in acetone for 1 h at 450 rpm using a 2:1 ball-to-powder ratio. An excess of Na<sub>2</sub>CO<sub>3</sub> (2% wt) was added to the mixture to compensate for the sodium evaporation that occurred during calcination. The mixture was left to dry in air and once dried, the powders were pressed as pellets (ca. 250 mg) under a load of 5 tons cm<sup>-2</sup>. The pellets were then calcined in a tube furnace under O<sub>2</sub> at 900 °C for 10 h, followed by slow cooling (10 °C min<sup>-1</sup>) in the tube furnace under an O<sub>2</sub> flow. Samples were quickly transferred to an argon-filled glovebox with < 0.1 ppm H<sub>2</sub>O/O<sub>2</sub>.

### **Characterisation**

Powder X-ray diffraction (XRD) data were recorded on a 9 kW Rigaku Smartlab diffractometer using Cu K $\alpha$  radiation ( $\lambda = 1.54051 \text{ \AA}$ ) for 12 h. Samples were run in customised sample holders with a Kapton window to avoid air/moisture exposure. Powder X-ray diffraction data were refined by conventional Rietveld methods using the GSAS package with the EXPGUI software interface<sup>14</sup>. Operando XRD studies were conducted with an operando XRD cell described elsewhere<sup>15</sup>. The measurements were performed at a current density of 10 mA g<sup>-1</sup> in the 2-4.5 V voltage window vs. Na<sup>+</sup>/Na. Colour maps were generated using MATLAB.

The chemical composition of the as-synthesised material was confirmed by inductively coupled plasma-optical emission spectroscopy (ICP-OES) using a PerkinElmer Optima 8000 ICP-OES. For the measurement, ca. 5mg of powder was dissolved in concentrated aqua regia and diluted to 1:100.

The microstructure of the as-synthesised material was characterised using scanning electron microscopy (SEM) (JEOL JSM-7800f, Japan) operating at 5 kV. Elemental analysis was performed using energy-dispersive X-ray spectroscopy (EDS) (Oxford Instruments, UK) at 12 kV. Samples were prepared by coating a uniform layer of the material onto carbon conductive tape.

Thermal analysis coupled with mass spectrometry was carried out on the pristine material (ca. 30 mg) using an alumina crucible as a holder under an argon flow. Measurements were performed using a NETZSCH Jupiter STA 449 F3 TGA coupled with a NETZSCH Aëolos QMS 403 D mass spectrometer to acquire simultaneous mass spectrometry data.

X-ray absorption near edge structure (XANES) data were collected on the B18 beamline at Diamond Light Source (UK). For the measurement, cast electrodes were cycled at different states of charge, extracted from the coin cells, rinsed with 3x 5 ml DMC (dimethyl carbonate) and dried at 80 °C under vacuum in the antechamber of the glovebox. Once dried, the electrodes were sealed in individual aluminium laminated pouches under vacuum to minimise air exposure during data acquisition. Measurements were performed at the Co and Mn K-edge energies in transmission mode, using gas-filled ionisation chambers to measure both incident and transmitted intensities. Co and Mn metal foils were used as internal standards. Three repetitions of each sample were measured. Athena software was used to sum the spectra, calibrate, extract the background and normalise the data<sup>16</sup>.

Soft X-ray absorption spectroscopy (XAS) and resonant inelastic X-ray scattering (RIXS) data were collected at BL27SU of the RIKEN/JASRI Spring8 synchrotron in Japan. Cast electrodes were prepared in an identical manner to the electrodes used in the XANES measurements. Electrodes were loaded onto adhesive copper tape and measured under  $10^{-6}$  Pa (high vacuum conditions).

Operando differential electrochemical mass spectrometry (DEMS) analysis was carried out to determine the presence and composition of the different gases evolved during galvanostatic cycling. The set up consisted of a quadrupole mass spectrometer (Thermo Fischer) equipped with a turbomolecular pump (Pfeiffer Vacuum) and mass-flow controllers (Bronkhorst). A 2-electrode type cell (ECC-Std from EL-CELL) with gas inlet and outlet ports was used for the operando measurements. The cell consisted of P2-NMMC (cathode), Na (anode) and 1 M NaPF<sub>6</sub> in PC (propylene carbonate, electrolyte). More details of the DEMS set-up are given in reference 5<sup>5</sup>.

### **Electrochemical characterisation**

Electrodes were prepared by mixing the active material with Super S carbon and a solution of 5 wt% PVDF (Polyvinylidene fluoride) in anhydrous NMP (N-Methyl-2-pyrrolidone) in a 75:15:10 weight ratio. Slurries of the mixtures were prepared by adding ca. 1.5 ml of NMP to the powdered mixture followed by constant stirring for 12 h. The slurry was cast onto an Al foil, that acts as a current collector, using a Doctor Blade. The casting process was carried out in an argon-filled glove box. The loading of the active material on the cast electrodes is 2-3 mg cm<sup>-2</sup>. The coated Al foil was dried at 80 °C under vacuum for 2 h using the heated antechamber of the glovebox. Electrodes of 19 mm in diameter were punched out of the Al foil and pressed under a load of 4 tons cm<sup>-2</sup>. Electrochemical tests were performed in CR2325 coin cells using 1 M NaPF<sub>6</sub> (99.99% Sigma Aldrich) in EC:DEC (1:1 vol%) (ethylene carbonate:diethyl carbonate) as the electrolyte solution, and sodium metal as the counter electrode. The electrolyte was dried using molecular sieves. Galvanostatic charge/discharge measurements were performed at different current densities in the 2-4.5 V vs. Na<sup>+</sup>/Na voltage window using a Neware Battery Tester. Cyclic voltammetric measurements were carried out

at a scan rate of  $0.1 \text{ mV s}^{-1}$  in the 2-4.5 V voltage window using an Iviumstat instrument (Alvatek).

## 2. Results and Discussion

### 2.1. Structure and composition

Figure 1b shows powder X-ray diffraction data of the as-prepared P2-NMMC material. All the Bragg diffraction lines (marked with  $hkl$  indices) can be indexed into a hexagonal lattice with a space group symmetry of  $P6_3/mmc$  (no. 194). No impurities were observed in the sample. From the structural refinement, the lattice parameters are calculated to be  $a = b = 2.87695(5) \text{ \AA}$  and  $c = 11.1824(4) \text{ \AA}$ , with volume  $V = 80.155(5) \text{ \AA}^3$ . Additional crystallographic information can be found in Table S1. The P2-NMMC structure is composed of alternate Na and MO layers ( $M = \text{Mg, Mn and Co}$ ), where Mg and transition metal ions occupy octahedral sites and Na ions occupy trigonal prismatic sites (Figure 1a). There are two distinctive prismatic sites in the sodium layer,  $\text{Na}_e$  and  $\text{Na}_f$  (in 2b and 2d Wyckoff sites, respectively), that share either edges or faces with the transition metal and Mg octahedra units ( $\text{MO}_6$ ). Transition metal and magnesium ions are randomly distributed in 2a sites, and oxygen atoms in 4f sites. 2b  $\text{Na}_e$  sites are more populated than 2d  $\text{Na}_f$  sites (ca. 2:1) due to the stronger electrostatic repulsions between  $\text{Na}^+$  ions located in face-shared sites with adjacent ions in the MO layer. The displacement parameters obtained for  $\text{Na}_e$  and  $\text{Na}_f$  ions, denoted by  $B_{iso}$  in Table S1, are  $3.2(3)$  and  $4.1(6) \text{ \AA}^2$ , respectively. A relatively high magnitude for these values, as was evidenced, has been previously associated with fast Na ion diffusion<sup>17</sup>. There is no evidence of long-range in-plane ordering between  $\text{Mg}^{2+}$  and  $\text{Mn}^{4+}$  ions neither in-plane  $\text{Na}^+$ /vacancy ordering given the absence of diffraction peaks in the  $20\text{-}28^\circ 2\theta$  region when using a Cu  $K_\alpha$  source<sup>8,18</sup>. The structural differences between P2-NMM and P2-NMMC may be explained by

the deviation from the 1:2 stoichiometric ratio between  $M^{2+}$  and  $M^{4+}$  ions in the latter compound. For instance, Lu et al. showed that the TM ordering in the  $P2\text{-Na}_{2/3}\text{Ni}_{1/3-x}\text{Co}_x\text{Mn}_{2/3}\text{O}_2$  ( $1/24 \leq x \leq 1/3$ ) system decreases upon substitution with  $\text{Co}^{3+}$  ions<sup>19</sup>. Figure 1c shows an SEM image of the as-prepared oxide, which showed disordered morphology composed of agglomerated platelet-like primary particles, with dimensions ranging from 1-3  $\mu\text{m}$  diameter and sub-micron thicknesses. EDS confirmed the presence of sodium, magnesium, manganese and cobalt in the sample (Figure S1). The composition of the targeted material was further validated using inductively coupled plasma (ICP)-optical emission spectroscopy (OES) (Table S2). Thermogravimetric analysis coupled with mass spectrometry (TGA/MS) were conducted in the as-prepared material to determine the thermal stability and amount of  $\text{Na}_2\text{CO}_3$  impurity<sup>20</sup>. TGA/MS data confirmed the stability of the P2-type material in the room temperature-750 °C temperature range, showing 1 wt% of mass loss with concomitant  $\text{CO}_2$  evolution, indicative of  $\text{Na}_2\text{CO}_3$  decomposition (Figure S2).  $\theta$

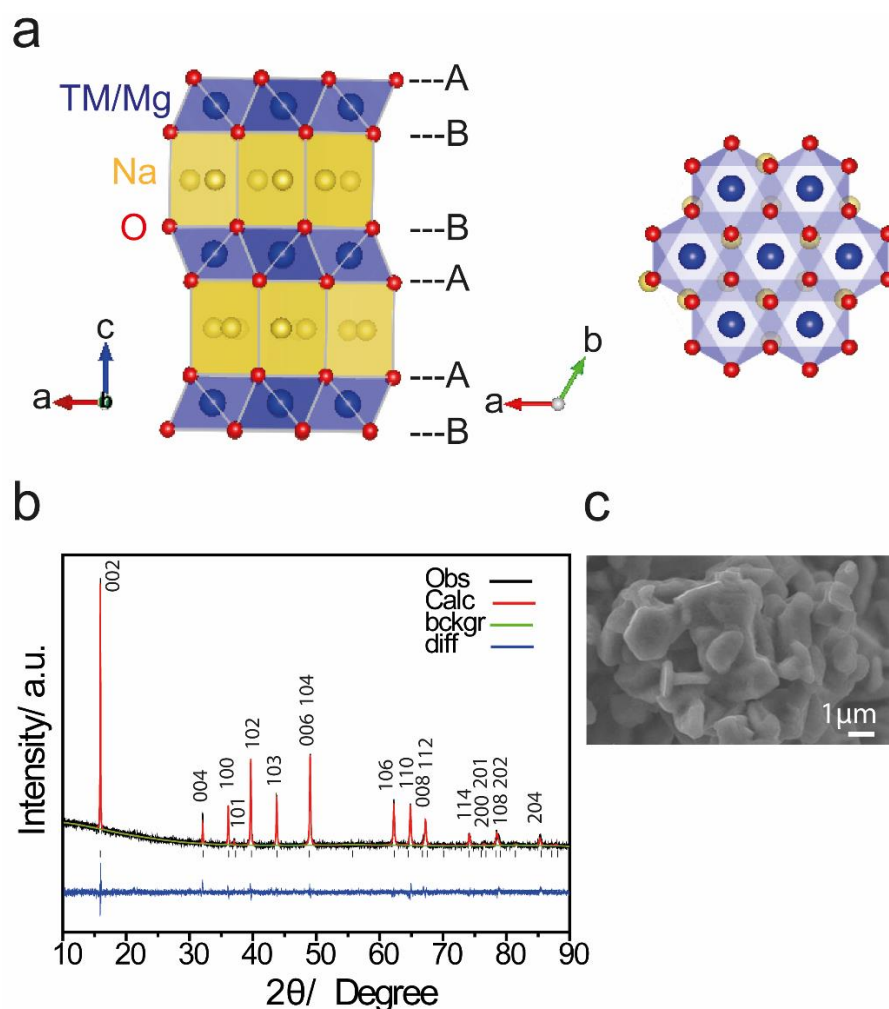


**Figure 1.** (a) Schematic representation of the P2-NMMC crystal structure viewed along the  $a$ -axis (left) and  $c$ -axis (right); (b) Rietveld refinement fit for P2-NMMC PXRD data ( $P6_3/mmc$  space group). The observed data (red), calculated data (green) and difference (blue) data and Bragg positions (black vertical bars) with  $hkl$  indices are shown; and (c) SEM image of the as-prepared P2-NMMC material.

## 2.2. Electrochemical properties

The electrochemical properties of P2-NMMC were examined in sodium half-cells at room temperature in the 2-4.5 V voltage window vs.  $\text{Na}^+/\text{Na}$  at the current density of  $C/20$  ( $1 C = 188 \text{ mAh g}^{-1}$  [equivalent to 0.66 Na ions removed per formula unit]) (Figure 2a). P2-NMMC delivers a specific capacity of  $162 \text{ mAh g}^{-1}$  at the end of the first charge, which corresponds to 0.58 Na ions extracted from P2-NMMC. Upon discharge to 2 V, a capacity of  $173 \text{ mAh g}^{-1}$  was

achieved, which corresponded to 0.62 Na ions inserted back in the structure. The P2-NMMC material shows an improved voltage hysteresis on the first cycle which is two times lower when  $x=0.125$  (0.54 Na ions extracted), when compared to the previously reported P2-NMM material<sup>8,9</sup> (Figure 2a). The calculated average discharge voltage of P2-NMMC is 2.9 V. Considering the specific capacity observed in the first discharge, the energy density of P2-NMMC is 495 Wh Kg<sup>-1</sup>. These values are comparable to other P2-layered materials such as Na<sub>2/3</sub>Fe<sub>1/2</sub>Mn<sub>1/2</sub>O<sub>2</sub> (523 Wh Kg<sup>-1</sup>)<sup>21</sup>. As shown in Figure 2a, the galvanostatic charge/discharge profiles of P2-NMMC during the first cycle involve a voltage plateau at 4.2 V, which has been attributed to various phase transitions occurring to P2-type materials such as P2-O2<sup>22</sup>, P2-OP4<sup>18</sup> and P2-“Z”<sup>23</sup>. In subsequent cycles, this plateau disappears with no significant loss in specific capacity, while the overall half-cell polarisation decreases (Figure S3). The absence of a plateau after the first cycle can be related to the abrupt decrease in current intensity of the anodic peak at ca. 4.3 V observed in the CV plots (Figure 2c). Galvanostatic charge/discharge data of the P2-NMMC material showed excellent capacity retention (87.7 %) and high Coulombic efficiency (99 %) after 40 cycles (Figure 2b), which may be attributed to the activation of the Mn<sup>3+</sup>/Mn<sup>4+</sup> redox couple upon cycling. This can be explained by the gradual increase in current density of the anodic (2.8 V) and cathodic (2.5 V) peaks observed in the CV data upon cycling<sup>24</sup> (Figure S4).

The rate performance of the P2-NMMC material is shown in Figure 2d. For each current step, five cycles were run to evaluate the rate capability of the material. P2-NMMC shows an acceptable rate capability, retaining 54 % of the first discharge capacity at a current density of 1C. The initial discharge capacity was fully retrieved when the current density returned to C/20. These results agree with the fast Na ion diffusion previously reported in P2-type compounds<sup>25</sup>.

Differential electrochemical mass spectrometry (DEMS) was used to explore gas evolution in the P2-NMMC compound during the first cycle. Data showed no evidence of direct O<sub>2</sub> evolution, similar to the P2-NMM material<sup>9</sup>. Only a small amount of CO<sub>2</sub> (0.013 moles CO<sub>2</sub>/mole P2-NMMC) was evolved before the start of the 4.23 V plateau and at the end of the first charge (Figure S5). The origin of CO<sub>2</sub> evolution has been previously studied in detail by Maitra et al. and can likely be attributed to unreacted Na<sub>2</sub>CO<sub>3</sub> and electrolyte decomposition<sup>9</sup>.

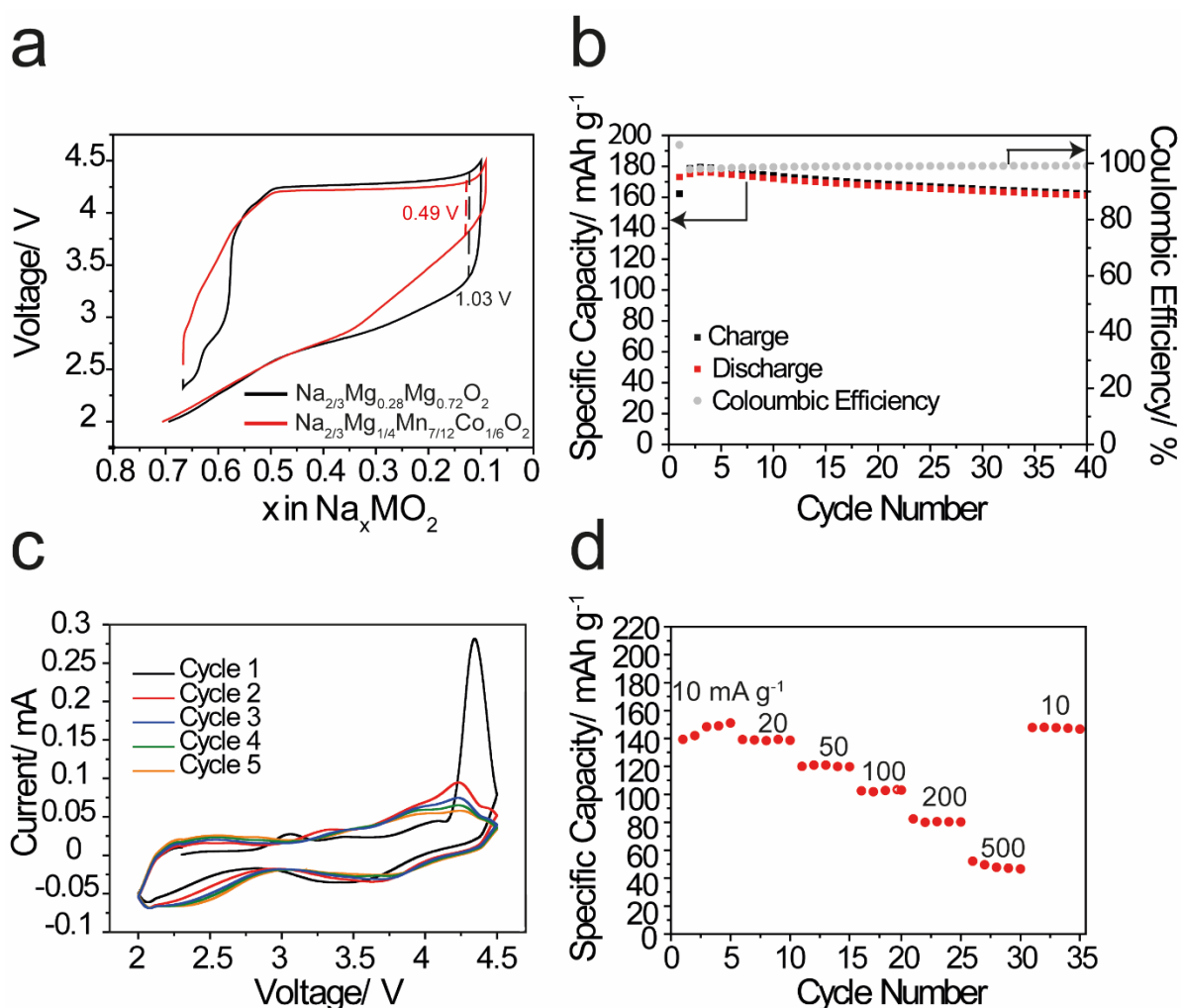


**Figure 2.** a) Voltage-composition curves (1<sup>st</sup> charge/discharge cycle) of P2-Na<sub>2/3</sub>Mg<sub>1/4</sub>Mn<sub>7/12</sub>Co<sub>1/6</sub>O<sub>2</sub> (red) and P2-Na<sub>2/3</sub>Mg<sub>0.28</sub>Mn<sub>0.72</sub>O<sub>2</sub> (black) in the 2-4.5 V voltage window at a current density of C/20; b) Cycling stability of P2-Na<sub>2/3</sub>Mg<sub>1/4</sub>Mn<sub>7/12</sub>Co<sub>1/6</sub>O<sub>2</sub> in the 2-4.5 V voltage window at a current density of C/20 over 40 cycles; c) Cyclic voltammogram

profiles at a scan rate of  $0.1 \text{ mV s}^{-1}$  in the 2-4.5 V voltage window of cycles 1-5; and d) Discharge capacities at different current densities in the 2-4.5 V voltage window.

### 2.3. Structural Changes on Cycling

To understand the structural evolution during the first charge/discharge process, operando XRD experiments were carried out, as shown in Figure 3. As the cathode material is charged ( $\text{Na}^+$  extracted) from the OCV state, the  $00l$  reflections of P2-NMMC shift to lower  $2\theta$  angles, whereas  $h00$  shift to higher angles up to 4.2 V indicating  $c$ -axis expansion and  $a$ -axis contraction. Contour maps in selected  $2\theta$  regions of the 002 and 100 reflections during the first cycle are shown in Figure 3a. This is known to occur due to increased electrostatic repulsion between the oxygen layers and the shortening of the TM-O bond lengths, respectively. The reverse trends were observed during discharge (i.e. sodium insertion). This trend has been previously observed in other P2-type materials<sup>17,22</sup>. When P2-NMMC is charged beyond 4.2 V (ca.  $50 \text{ mAh g}^{-1}$ ), the load curve shows a plateau that continues until the end of charge (Figure 3b), indicative of a two-phase behaviour. Within this range, the (002) reflection shows a continuous decrease in the intensity and increase in broadening until the end of charge indicating a decrease in the long-range ordering caused by deviations from the ideal P2 stacking sequence. This is concomitant to the presence of a new broad diffraction peak at  $17.3^\circ 2\theta$  which has been previously observed in other P2 compounds at high desodiation levels<sup>22</sup>. Upon Na insertion, the Bragg peaks of the P2 structure are regained, without any new diffraction peaks present, showing a reversible process.

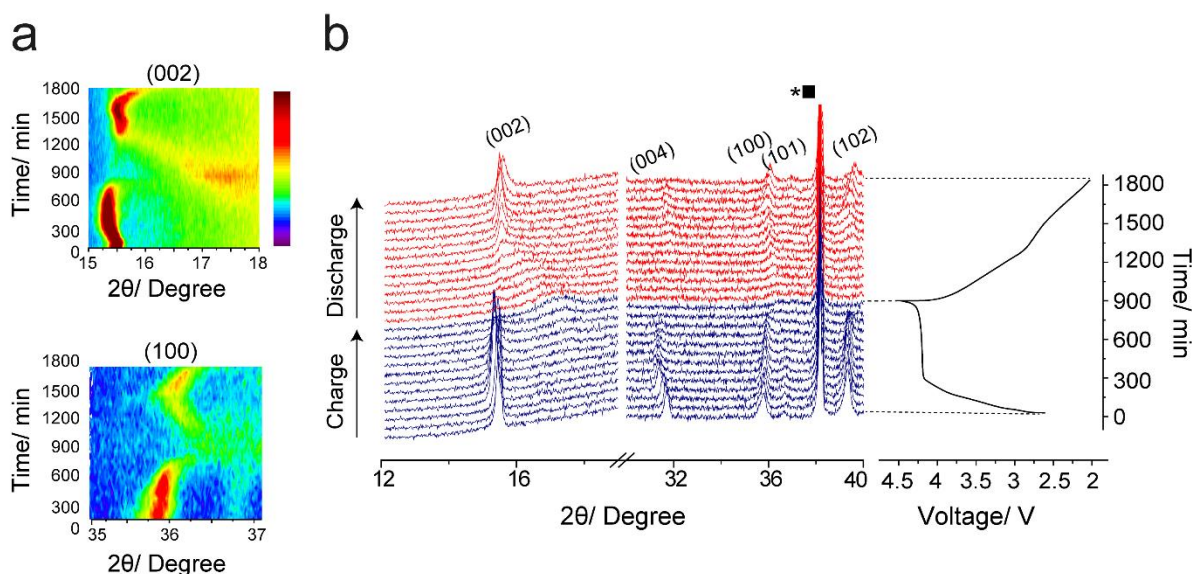


**Figure 3.** a) Operando XRD colour maps monitoring the evolution of the 002 and 100 reflections during the first charge/discharge cycle of P2-NMMC. The colour scale represents reflection intensity. b) XRD data of P2-NMMC in a selected  $2\theta$  region (12-40°  $2\theta$ ) recorded under operando conditions with corresponding charge/discharge voltage profile. Bragg peaks indicated with (■) correspond to Be window and the (\*) symbol corresponds to Al. Electrochemical data were collected using a current density of  $10 \text{ mA g}^{-1}$  in the 2-4.5 V vs.  $\text{Na}^+/\text{Na}$  voltage window.

X-ray absorption (XAS) spectroscopy measurements at the TM and O K-edges were conducted at different charge/discharge depths to investigate the charge compensation mechanism during Na extraction and insertion. Figures 4(a-d) show normalised Co and Mn K-edge XANES spectra (7.112 and 6.537 keV, respectively) at different states of charge.  $\text{LiCoO}_2$  ( $\text{Co}^{3+}$ ),  $\text{Mn}_2\text{O}_3$  ( $\text{Mn}^{3+}$ ) and  $\text{MnO}_2$  ( $\text{Mn}^{4+}$ ) were used as standards. By direct comparison with the K-edge absorption energies of the standards (using the first derivative of the white line), it was evident that pristine P2-NMMC consisted of trivalent Co and tetravalent Mn ions, as expected from the calculated oxidation states. The heating temperature (900 °C), oxidative

atmosphere, and the slow cooling rate used in the reaction ( $10\text{ }^{\circ}\text{C min}^{-1}$ ) may favour the higher valence state of  $\text{Mn}^{4+}$  and  $\text{Co}^{3+}$  ions.

An absorption energy shift in the Co K-edge (1s-4p) of 1.2 eV was observed during charge until the start of the 4.23 V plateau (Figure 4a), indicating that  $\text{Co}^{3+}$  ions are oxidised in this voltage window<sup>26</sup>. The experimental capacity in this voltage window ( $50\text{ mAh g}^{-1}$ ) is consistent with the theoretical capacity expected from the oxidation of 0.167 moles  $\text{Co}^{3+}$  to  $\text{Co}^{4+}$  in P2-NMMC, i.e.  $47\text{ mAh g}^{-1}$ . No further changes in the Co K-edge were observed during sodium extraction. On discharge, a shift in the K-edge to lower energies was observed from ca. 3 V to 2 V, showing that  $\text{Co}^{4+}$  ions were reduced back to the original  $\text{Co}^{3+}$  state observed in the pristine material (Figure 4b). Interestingly, these data indicate that the reduction process occurs at a substantially lower voltage than the oxidation of the cobalt ions.

No dramatic changes in the absorption energies were observed in the Mn K-edge (1s-4p) during the first charge and discharge, indicating that the tetravalent oxidation state of Mn stays unchanged during the first cycle (Figures 4c and 4d). Both Mn spectra (on charge and discharge) exhibit a pre-edge absorption, which is assigned to a formally electric-dipole forbidden transition from 1s to 3d in an ideal octahedral symmetry and appears by 3d-4p orbital mixing caused by the distortion of  $\text{MnO}_6$  octahedra. The Mn K pre-edge feature has been considered a relatively good indicator of the oxidation state of the Mn ion<sup>27,28</sup>. Our pre-edge data did not show any shifts on Na extraction/insertion, as can be seen in the insets of Figures 4c-d.

Soft X-ray absorption data of the P2-NMMC material were collected at selected states of charge to study redox processes occurring on the oxygen anion (Figure 4e). The O K-edge XAS data shows the most prominent change in absorbance in the pre-edge (525-535 eV range)

between the samples charged at 4.2 V and 4.5 V. After discharge to 2 V, the normalised spectrum was identical to that of the pristine electrode, indicating a reversible process.

RIXS spectra were measured at a single excitation energy of 531.5 eV (Figure 4f). Furthermore, RIXS data showed the presence of a peak at 524 eV (highlighted in yellow in Figure 4f) on the sample charged to 4.5 V, which represents an emission from the O 2p valence band, which disappeared after discharge to 2 V. These observations may be attributed to O-redox behaviour in P2-NMMC and are consistent with data previously reported on  $\text{Na}_{2/3}\text{Mg}_{0.28}\text{Mn}_{0.72}\text{O}_2$ <sup>9</sup>.

In conclusion, combined hard and soft XANES data show that 1) the  $\text{Co}^{3+}/\text{Co}^{4+}$  redox couple is the only TM active couple in P2-NMMC in the 2-4.5 V voltage window during the first cycle, and 2) the capacity observed after the plateau (ca. 115 mAh g<sup>-1</sup>) may be associated with anionic redox processes taking place during sodium extraction.

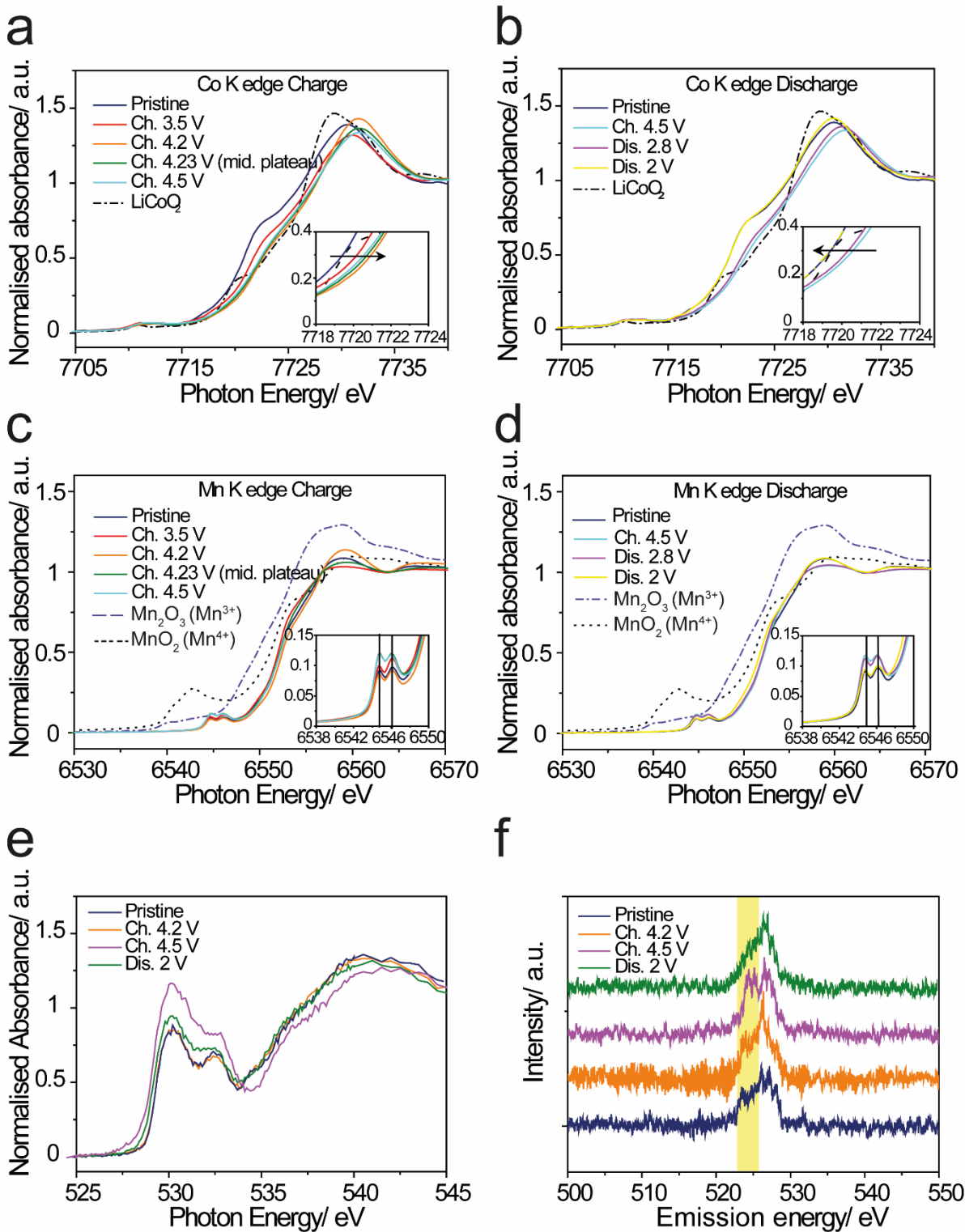


**Figure 4.** XANES data of the P2-NMMC cathode material, showing the evolution of Co K-edge during charge (a) and discharge (b); and the evolution of the Mn K-edge during charge (c) and discharge (d). K-energies at the normalised absorbance of 0.3 are shown as an inset of a) and

b); Pre-edge for Mn is shown as an inset of c) and d). For comparison, XANES spectra of LiCoO<sub>2</sub> (Co<sup>+3</sup>), Mn<sub>2</sub>O<sub>3</sub> (Mn<sup>3+</sup>) and MnO<sub>2</sub> (Mn<sup>4+</sup>) reference materials are shown; (e) SXAS O K-edge spectra of P2-NMMC collected at different states of charge in total fluorescence yield mode; and (f) RIXS on the O K-edge of P2-NMMC with an excitation energy of 531.5 eV.

## Conclusions

In this work, we have reported the synthesis of a new P2-type material, Na<sub>2/3</sub>Mg<sub>1/4</sub>Mn<sub>7/12</sub>Co<sub>1/6</sub>O<sub>2</sub>, using solid-state methods. The material, which crystallises in the *P6<sub>3</sub>/mmc* space group, shows a disordered distribution of Mg<sup>2+</sup>/Mn<sup>4+</sup>/Co<sup>3+</sup> in the transition metal layer across the 2a sites, as observed in the powder X-ray diffraction data. This contrasts with the crystal structure of the Co-free analogue with space group *P6<sub>3</sub>* (P2-NMM), which shows an ordered arrangement (i.e. honeycomb ordering) of Mg<sup>2+</sup>/Mn<sup>4+</sup> in the transition metal layer. Galvanostatic charge/discharge studies showed specific capacities as high as 173 mAh g<sup>-1</sup> in the 2-4.5 V voltage window. Furthermore, galvanostatic data allowed us to determine that the substitution of Co<sup>3+</sup> ions for Mg<sup>2+</sup> and Mn<sup>3+</sup>/Mn<sup>4+</sup> in the transition metal layer of P2-NMM improves the first cycle voltage hysteresis. Electrochemical data corroborated our X-ray diffraction data showing an initial solid-solution followed by a bi-phasic regime where an OP4-like phase exists. Confirmation of the O-redox occurring across the 4.2 V plateau was obtained by a combination of X-ray absorption spectroscopy along with resonant X-ray inelastic scattering.

## Conflicts of interest

There are no conflicts to declare.

## Acknowledgements

NTR would like to thank Lancaster University, the Royal Society (RG170150) and the Faraday Institution (FIRG018) for financial support. PGB would like to thank the Engineering and Physical Sciences Research Council (EPSRC) and the Henry Royce Institute for capital equipment [EP/R010145/1]. We would like to thank Dr Claire Villevieille for providing access to the operando XRD cell. We acknowledge the Science and Technology Facilities Council (STFC) for access to B18 beamtime at the Diamond Light Source. The authors are grateful to G. Cibirin for contributing to the collection of the XAS data.

## References

- [1] Schubert, C. Making fuels for the future. *Nature* **2011**, 474, 531–533.
- [2] Eftekhari, A.; Kim, D.-W. Sodium-ion batteries: New opportunities beyond energy storage by lithium. *J. Power Sources* **2018**, 395, 336–348.
- [3] Delmas, C. Sodium and Sodium-Ion Batteries: 50 Years of Research. *Adv. Energy Mater.* **2018**, 8(17), 1703137.
- [4] Kubota, K.; Kumakura, S.; Yoda, Y.; Kuroki, K.; Komaba, S. Electrochemistry and Solid-State Chemistry of NaMeO<sub>2</sub> (Me = 3d Transition Metals). *Adv. Energy Mater.* **2018**, 8(17), 1703415.
- [5] Luo, K.; Roberts, M. R.; Hao, R.; Guerrini, N.; Pickup, D. M.; Liu, Y. S.; Edström, K.; Guo, J. H.; Chadwick, A. V.; Duda, L. C.; Bruce, P. G. Charge-compensation in 3d-transition-metal-oxide intercalation cathodes through the generation of localized electron holes on oxygen. *Nat. Chem.* **2016**, 8, 684–691.

- [6] Seo, D. H.; Lee, J.; Urban, A.; Malik, R.; Kang, S.; Ceder, G. The Structural and Chemical Origin of the Oxygen Redox Activity in Layered and Cation-Disordered Li-Excess Cathode Materials. *Nat. Chem.* **2016**, 8(7), 692–697.
- [7] Ma, C.; Alvarado, J.; Xu, J.; Clément, R. J.; Kodur, M.; Tong, W.; Grey, C. P.; Meng, Y. S. Exploring Oxygen Activity in the High Energy P2-Type  $\text{Na}_{0.78}\text{Ni}_{0.23}\text{Mn}_{0.69}\text{O}_2$  Cathode Material for Na-Ion Batteries. *J. Am. Chem. Soc.* **2017**, 139(13), 4835–4845.
- [8] Yabuuchi, N.; Hara, R.; Kubota, K.; Paulsen, J.; Kumakura, S.; Komaba, S. New Electrode Material for Rechargeable Sodium Batteries: P2-Type  $\text{Na}_{2/3}[\text{Mg}_{0.28}\text{Mn}_{0.72}]\text{O}_2$  with Anomalously High Reversible Capacity. *J. Mater. Chem. A* **2014**, 2, 16851-16855.
- [9] Maitra, U.; House, R. A.; Somerville, J. W.; Tapia-Ruiz, N.; Lozano, J. G.; Guerrini, N.; Hao, R.; Luo, K.; Jin, L.; Pérez-Osorio, M. A.; et al. Oxygen Redox Chemistry without Excess Alkali-Metal Ions in  $\text{Na}_{2/3}[\text{Mg}_{0.28}\text{Mn}_{0.72}]\text{O}_2$ . *Nat. Chem.* **2018**, 10(3), 288–295.
- [10] Sathiya, M.; Rouse, G.; Ramesha, K.; Laisa, C. P.; Vezin, H.; Sougrati, M. T.; Doublet, M. L.; Foix, D.; Gonbeau, D.; Walker, W.; et al. Reversible Anionic Redox Chemistry in High-Capacity Layered-Oxide Electrodes. *Nat. Mater.* **2013**, 12(9), 827–835.
- [11] McCalla, E.; Abakumov, A. M.; Saubanère, M.; Foix, D.; Berg, E. J. et al. Visualization of O–O peroxo-like dimers in high-capacity layered oxides for Li-ion batteries. *Science* **2015**, 350, 1516–1521.
- [12] Assat, G.; Delacourt, C.; Corte, D. A. D.; Tarascon, J.-M. Editors' Choice—Practical Assessment of Anionic Redox in Li-Rich Layered Oxide Cathodes: A Mixed Blessing for High Energy Li-Ion Batteries. *J. Electrochem. Soc.* **2016**, 163, A2965–A2976.

- [13] Assat, G.; Tarascon, J. M. Fundamental understanding and practical challenges of anionic redox activity in Li-ion batteries. *Nat. Energy* **2018**, 3, 373–386.
- [14] Larson, A. C.; Von Dreele, R. B. GSAS General Structure Analysis System, *Los Alamos National Laboratory Report LAUR* **1994**, 86-748; Toby, B. H. EXPGUI, a graphical user interface for GSAS. *J. Appl. Cryst.* **2001**, 34, 210–213.
- [15] Bleith, P.; Kaiser, H.; Novák P.; Villevieille, C. In-situ X-ray diffraction of  $\text{Fe}_{0.5}\text{TiOPO}_4$  and  $\text{Cu}_{0.5}\text{TiOPO}_4$  as electrode material for sodium-ion batteries. *Electrochim. Acta* **2015**, 176, 18–21.
- [16] Ravel, B.; Newville, M. ATHENA, ARTEMIS, HEPHAESTUS: data analysis for X-ray absorption spectroscopy using IFEFFIT. *J. Synchrotron Radiat.* **2005**, 12, 537–541.
- [17] Singh, G.; Tapia-Ruiz, N.; Lopez Del Amo, J. M.; Maitra, U.; Somerville, J. W.; Armstrong, A. R.; Martinez De Ilarduya, J.; Rojo, T.; Bruce, P. G. High Voltage Mg-Doped  $\text{Na}_{0.67}\text{Ni}_{0.3-x}\text{Mg}_x\text{Mn}_{0.7}\text{O}_2$  ( $x = 0.05, 0.1$ ) Na-Ion Cathodes with Enhanced Stability and Rate Capability. *Chem. Mater.* **2016**, 28(14), 5087–5094.
- [18] Tapia-Ruiz, N.; Dose, W. M.; Sharma, N.; Chen, H.; Heath, J.; Somerville, J. W.; Maitra, U.; Islam, M. S.; Bruce, P. G. High Voltage Structural Evolution and Enhanced Na-Ion Diffusion in  $\text{P2-Na}_{2/3}\text{Ni}_{1/3-x}\text{Mg}_x\text{Mn}_{2/3}\text{O}_2$  ( $0 \leq x \leq 0.2$ ) Cathodes from Diffraction, Electrochemical and Ab Initio Studies. *Energy Environ. Sci.* **2018**, 11(6), 1470–1479.
- [19] Lu, Z.; Donaberger, R. a.; Dahn, J. R. Superlattice Ordering of Mn, Ni, and Co in Layered Alkali Transition Metal Oxides with P2, P3, and O3 Structures. *Chem. Mater.* **2000**, 12(12), 3583–3590.

- [20] Duffort, V.; Talaie, E.; Black, R.; Nazar, L. F. Uptake of CO<sub>2</sub> in Layered P2-Na<sub>0.67</sub>Mn<sub>0.5</sub>Fe<sub>0.5</sub>O<sub>2</sub>: Insertion of Carbonate Anions. *Chem. Mater.* **2015**, 27(7), 2515–2524.
- [21] Somerville, J. W., House, R. A., Tapia-Ruiz, N., Sobkowiak, A., Ramos, S., Chadwick, A. V., Roberts, M. R., Maitra, U., & Bruce, P. G. (2018). Identification and characterisation of high energy density P2-type Na<sub>2/3</sub>[Ni<sub>1/3-y/2</sub>Mn<sub>2/3-y/2</sub>Fe<sub>y</sub>]O<sub>2</sub> compounds for Na-ion batteries. *J. Mater. Chem. A* **2018**, 6, 5271.
- [22] Lu, Z.; Dahn, J. R. In Situ X-Ray Diffraction Study of P2-Na<sub>2/3</sub>Ni<sub>1/3</sub>Mn<sub>2/3</sub>O<sub>2</sub>. *J. Electrochem. Soc.* **2001**, 148(11), A1225.
- [23] a) Mortemard De Boisse, B.; Carlier, D.; Guignard, M.; Bourgeois, L.; Delmas, C. P2-NaxMn<sub>1/2</sub>Fe<sub>1/2</sub>O<sub>2</sub> Phase Used as Positive Electrode in Na Batteries: Structural Changes Induced by the Electrochemical (De)Intercalation Process. *Inorg. Chem.* **2014**, 53(20), 11197–11205.
- b) Somerville, J. W.; Sobkowiak, A.; Tapia-Ruiz, N.; Billaud, J.; Lozano, J. G.; House, R. A.; Gallington, L. C.; Ericsson, T.; Häggström, L.; Roberts, M. R.; Maitra U.; Bruce, P.G. *Energy Environ. Sci.* **2019**, 12(7), 2223-2232
- [24] Park, K.; Han, D.; Kim, H.; Chang, W. S.; Choi, B.; Anass, B.; Lee, S. Characterization of a P2-Type Chelating-Agent-Assisted Na<sub>2/3</sub>Fe<sub>1/2</sub>Mn<sub>1/2</sub>O<sub>2</sub> Cathode Material for Sodium-Ion Batteries. *RSC Adv.* **2014**, 4(43), 22798–22802.
- [25] Mo, Y.; Ong, S. P.; Ceder, G. Insights into Diffusion Mechanisms in P2 Layered Oxide Materials by First-Principles Calculations. *Chem. Mater.* **2014**, 26(18), 5208–5214.
- [26] Kim, M.G.; Yo, C.H. X-ray Absorption Spectroscopic Study of Chemically and Electrochemically Li ion Extracted Li<sub>y</sub>Co<sub>0.85</sub>Al<sub>0.15</sub>O<sub>2</sub> compounds, *J. Phys. Chem. B* **1999**, 103(31) 6457–6465.

[27] Manceau, A.; Gorshkov, A. I.; Drits, V. A. Structural chemistry of Mn, Fe, Co, and Ni in manganese hydrous oxides, *Amer. Mineral.* **1992**, 77, 1133-1143.

[28] Ammundsen, B.; Jones, D. J.; Rozière, J.; Burns, G. R. Effect of Chemical Extraction of Lithium on the Local Structure of Spinel Lithium Manganese Oxides Determined by X-Ray Absorption Spectroscopy. *Chem. Mater.* **1996**, 8(12), 2799–2808.